ORIGINAL RESEARCH ARTICLE

Influence of a Stationary Shoulder Friction Stir Welding Tool on the Mechanical and Corrosion Properties of AA2024 Aluminum Alloy Joints at Different Parameter Values

Sunil Sinhmar [iD] and Dheerendra Kumar Dwivedi

Sound weld joints of similar AA2024 aluminum alloy plates of 6 mm were achieved unprecedentedly at different rotational (386-1216 rpm) and traverse speeds (13-90 mm/min) using an indigenously developed stationary shoulder friction stir welding (SSFSW) tool. Results indicate a smooth and bowl-shaped symmetrical nugget zone (NZ) with fine equiaxed grains. The grains as well as the nugget zone width vary with the speed variation. A change of 16% in the width of NZ is observed with an increase in traverse speed from 13 to 90 mm/min. The SSFSW tool reduces the width of the weakest region of the weld joint, known as the heat-affected zone, by almost 50%. The SSFSW joint produced at 931-90 mm/min shows the highest value (101 HV) of the minimum hardness region as compared to other parameters. The SSFSW tool shifts the weakest region toward the NZ, as substantiated by the fracture location of the tensile samples. In addition, SSFSW joints show higher corrosion resistance in NZ due to recrystallized fine grains as compared to HAZ. The SSFSW tool reduces the width of the most severely corrosion-affected region and, hence, improves the corrosion resistance of the joint.

1. Introduction

Welding is an important joining technique and is tremendously used in manufacturing industries. Generally, weld joints experience heterogeneities in the microstructure, which form various regions in the joint (Ref 1). The nugget zone, thermomechanical affected zone, and HAZ experience different levels of thermal effect and exhibit different microstructures (Ref 2). The base metal remains unaffected by the microstructural changes on both the retreating and advancing sides (Ref 3). Joining aluminum alloys with similar as well as dissimilar materials is getting more and more attention, especially due to weight reduction requirements (Ref 4). However, fusion weld joints of aluminum alloys are prone to various defects such as solidification cracking, porosity, and lack of penetration (Ref 5). Therefore, being a solid-state process, FSW has been started to be used for the joining of such alloys that are problematic to weld with the fusion welding processes (Ref 6). Friction-based joining processes are capable of producing the welds at a comparatively high energy efficiency (Ref 7).

Generally, in the case of weld joints, especially the heat-treatable aluminum alloys, the heat-affected zone (HAZ) is found to be the rigorously affected region, and this is also true for friction stir welding (Ref 8). The dissolution and coarsening of the strengthening precipitates lead to the mechanical and electrochemical weakening of the HAZ (Ref 9). In view of this, a novel kind of FSW tool named the stationary shoulder friction stir welding tool was developed to reduce the width of HAZ (Ref 10).

In FSW, parameters like the selection of the proper tool, the dimensions of various parts of the tool, and the design of the tool significantly affect the performance of the weld joint (Ref 11). Recently, the use of the SSFSW tool to produce weld joints has increased significantly. However, several of the issues encountered while using the SSFSW tool, like the extruded material penetrating the tool body, were noted (Ref 12). The minor gap between the stationary shoulder and rotating part allows the flow of plastically deformed material from the weld joint, which in turn leads to the cavity defect (Ref 13). Therefore, an indigenously developed SSFSW tool, harnessed with the special characteristic of self-removal of penetrated material from the tool body, has been used (Ref 14).

In the initial phase of SSFSW, the stationary shoulder tool was used for the corner joint (Ref 15). The higher cooling rate of the SSFSW joint significantly controls the coarsening of precipitates (Ref 16). Thus, the rate of cooling significantly affects the strength and behavior of the weld joint (Ref 17). The stationary shoulder-assisted tool helped in the rapid cooling and simultaneously performed rolling action during FSW, which in turn helped to reduce the tensile residual stresses in the weld

Sunil Sinhmar, Materials Science and Engineering, Indian Institute of Technology Kanpur, Kanpur, Uttar Pradesh 208016, India; and **Dheerendra Kumar Dwivedi**, Mechanical and Industrial Engineering Department, Indian Institute of Technology Roorkee, Roorkee 247667, India. Contact e-mails: ssinhmar@iitk.ac.in and dkd04fme@iitr.ac.in.

joint (Ref 18). The tensile residual stress in a SSFSW joint was found to be 50% lower than that in the CFSW joint of 6xxx series aluminum alloy (Ref 19). The weld thermal cycle and heat input of conventional and stationary shoulder FSW/FSP joints were analyzed, and it was found that the SSFSW tool resulted in low heat input and a narrow HAZ (Ref 20). The effect of variation in the traverse speed of the SSFSW tool on the lap joint feature was observed in a 2024 aluminum alloy (Ref 21). The shear failure load first increased and then decreased with an increase in the traverse speed. The effect of rotational speeds on the SSFSW lap joint was investigated, and the maximum shear load was observed at a rotational speed of 1400 rpm (Ref 22). The variation of rotational speed using the SSFSW tool on a T-joint of 2A14 aluminum alloy exhibited surface groove defects, especially at high speeds (Ref 23). The microstructural homogeneity of the Al-Cu alloy weld joint using the SSFSW tool was found to be better than that of the CFSW joint (Ref 24). The effective strain and softness of the SSFSW joint were also reduced as compared to the conventional joint.

The corrosion behavior of the stir zone of the FSW joint was found to be highly dependent on the rotation speed in the case of heat-treatable aluminum alloys (Ref 25). A critical review of the SSFSW tool and its comparison with the CFSW and bobbin tools is also available in the literature, which suggests the effectiveness of the SSFSW tool to produce low heat input joints (Ref 26).

According to the literature, only a small number of experiments have been carried out to create SSFSW joints at a variety of parameters. This technique has a huge future scope to join low-melting materials and dissimilar materials due to its capability of concentrating heat input into the weld joint. Therefore, in view of its potential use in future applications, a thorough study of different parameters is required. The present study aims to investigate the capability of the SSFSW tool to produce sound weld joints of AA2024 aluminum alloy at various rotational and traverse speed parameters. This study also targets finding the effect of parameter changes on the width of HAZ using the SSFSW tool. The electrochemical behavior of the weld joints is an important aspect from a performance point of view and has not been profoundly addressed for the SSFSW joints so far. Therefore, the mechanical and electrochemical behavior of the SSFSW joints has been examined and juxtaposed with that of the CFSW joint. The effect of the speed parameters on the nugget zone as well as the HAZ of the FSW joint using the SSFSW tool is thoroughly studied in this work.

2. Material and Methods

The aluminum-copper alloy (AA2024) was used for the FSW using conventional and stationary shoulder tools in this study. The chemical composition and mechanical properties of

AA2024 are given in Table 1. The thickness of the plate was 6 mm. The length and width of the plate were 100 and 27.5 mm, respectively. A vertical milling machine with a 15-horsepower motor was used for the welding. The welding was performed using a stationary shoulder FSW tool at four disparate rotary speeds at a fixed traverse speed and four disparate traverse speeds at a fixed rotary speed (Table 2). The FSW was also performed using a conventional tool to compare the performance with the SSFSW joint. Conventional FSW was carried out at two extreme rotational and traverse speeds (highest and lowest), which were used for the SSFSW as shown in Table 3. The shoulder during CFSW was rotating, whereas it was non-rotating during SSFSW. The schematic of the SSFSW process along with process elements and the real images of both types of tools are shown in Fig. 1. The diameter of the shoulder in both cases was 16 mm. The diameters of the pin were 6 mm and 3 mm (top and bottom), with a length of 5.8 mm. The tilt angle in both cases was kept at 1.5°. In the case of the SSFSW, the dwell time was kept at 90 s, whereas it was 60 s during the CFSW.

The coupons for the macrostructure and microstructure analysis were produced along the transverse direction of the weld and polished to a mirror finish. Coupons were etched by Keller's reagent (for 25 s) prior to the microstructural analysis. The FESEM analysis along with the EDS were performed to recognize the precipitates in the base metal AA2024. The microhardness profile was measured using Vicker's microhardness tester on the lateral side of the weld (ASTM E384). Dwell time, load, and space between two successive indentations were 10 s, 100 g and 0.5 mm, respectively. The specimens for the tensile tests were extracted according to ASTM E8 along the lateral cross-section by keeping the pin-stirred region of the weld at the center of the tensile sample. Instron's UTM of 100 kN capacity was used for the testing at room temperature. The crosshead speed of the machine during the test was 0.5 mm/min. Fractured samples after the tensile test were analyzed using FESEM. The direct current-based corrosion test, also known as the potentiodynamic polarization test, was carried out to study the corrosion behavior of the samples. The Tafel curves of the samples welded at various speed parameters were plotted, and the corroded surface was analyzed using scanning electron microscopy. The electrochemical experiments according to ASTM G102 were executed in a 3.5% NaCl environment using Gamry's potentiostat (Model-1000) equipped with DC105 software. The schematic shown in Fig. 2 shows a three-electrode setup for the corrosion test. The parameters used for the corrosion test were − 0.25 to 0.25 volts (potential range) and 1 millivolt per second (scan rate). The open-circuit delay time for each test was 1800 s. The schematic shown in Fig. 3 demonstrates the locations of the samples extracted from the weld joint for microstructural, microhardness, tensile, and electrochemical analysis.

**Table 1 Chemical composition and mechanical properties of AA2024**

Elements	Cu	Si	Fe	Mn	Mg	Zn	Al	UTS, MPa	Elongation, %
								Mechanical properties	
wt.%	4.4	0.3	0.4	0.5	1.6	0.18	Balance	469	19

Table 2 Speed parameters used for the SSFSW of AA2024 aluminum alloy

	Rotational speeds				Traverse speeds			
rpm	386	664	931	1216	931	931	931	931
mm/min	13	13	13	13	13	30	66	90

Table 3 Speed parameters used for the conventional FSW of AA2024 aluminum alloy

	Rotational speeds		Traverse speeds	
rpm	386	1216	931	931
mm/min	13	13	13	90
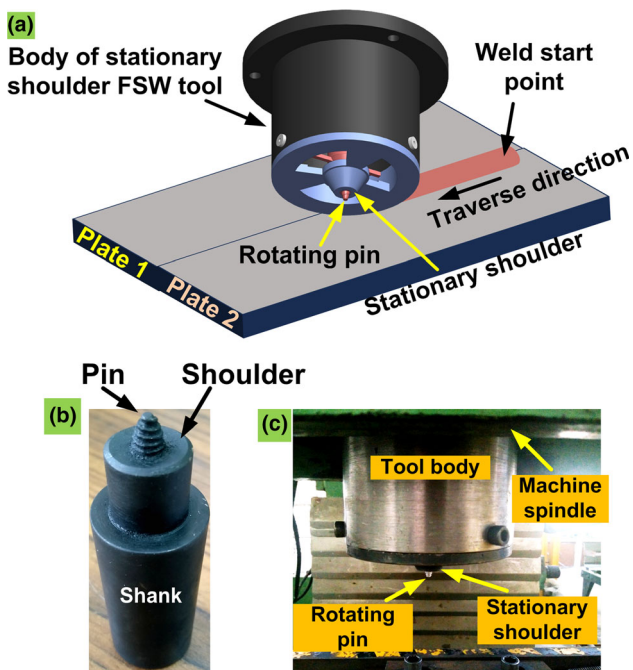
Fig. 1 Shows (a) schematic of SSFSW process, (b) image of conventional FSW tool, and (c) image of SSFSW tool
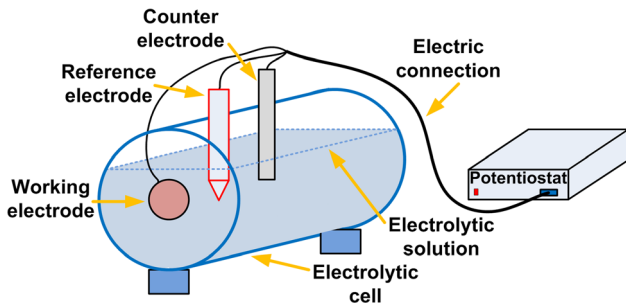
Fig. 2 Schematic shows a three-electrode setup for corrosion test
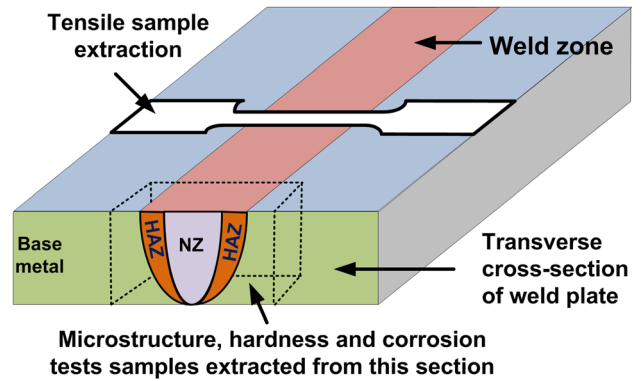
Fig. 3 Schematic shows the locations of various test samples extracted from weld joint

3. Results and Discussion

3.1 Macrostructure

The plates welded by SSFSW and CFSW tools at 931 rpm and 13 mm/min are shown in Fig. 4(a) and (b), respectively. Low traverse speeds are found to be more effective for producing a smooth weld surface. On the contrary, a high traverse speed weld joint lacks the high axial downward force required to produce an ideal smooth surface. Streaks (also called the wake effect) at the upper surface of the plates due to rotation of the shoulder were observed in the case of the CFSW joint (Fig. 4b), and this resulted in a rougher surface than the SSFSW joint. A stationary shoulder tool, which just slides over the weld plate without rotation, prevents the plasticized material under the shoulder from escaping. This provides the sealing effect, which in turn results in a smooth surface without flash. Plasticized material accumulated at the edges of the shoulder movement region over the top surface of the plate in the CFSW joint, but this was not evidenced in the case of the SSFSW joint.

Macroimages of the transverse cross-section of SSFSW and CFSW joints at disparate speed parameters are shown in Fig. 5. The variation in the shape of the nugget zone (pin-stirred region) was not significant except at 386 rpm (the lowest rotational speed) in the case of SSFSW joints. However, variation in the width of NZ was observed in the case of SSFSW joints. The width of NZ was measured at mid-thickness. The observed values of the width of the NZ of the weld joints produced at 13, 30, 66, and 90 mm/min (at 931 rpm) were 6.174, 5.586, 5.233, and 5.174 mm, respectively. The width of the NZ of the weld joints produced at 386, 664, and 1216 rpm (at 13 mm/min) was 5.703 mm, 5.586 mm, and 5.703 mm, respectively. The width of the NZ was reduced with an increase in traverse speed of 931 rpm. However, no uniform variation in the width of NZ with a change in rotational speed was observed. Low and high rotational speeds resulted in the same width, whereas 931 rpm resulted in a wider NZ than the remaining rotational speeds. Any tunnel or root defect was not observed in SSFSW joints, but a lack of mixing at the top part (shoulder active region) was witnessed in weldments produced at high traverse speeds. A defect in the middle of NZ
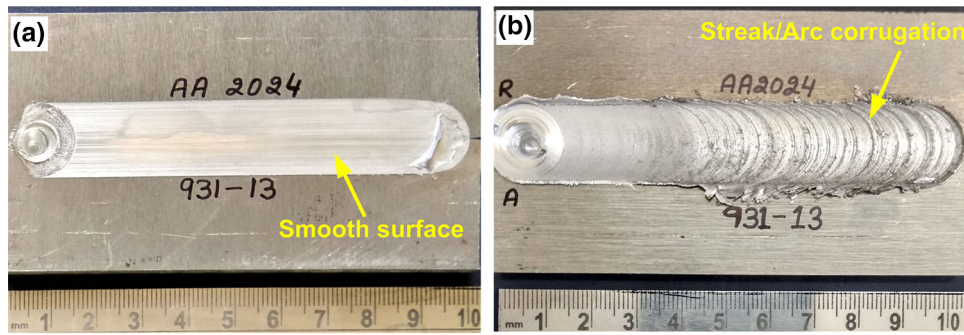
Fig. 4 Photographs of the weld plates joined at low traverse speed by (a) SSFSW tool, and (b) CFSW tool
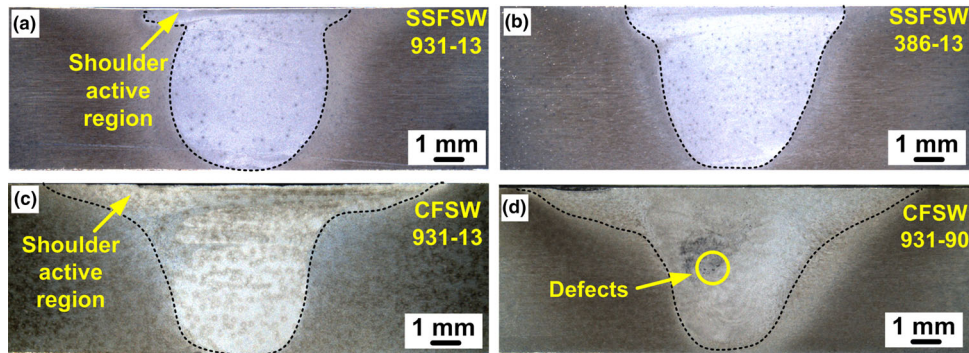

Fig. 5 Stereo images of the lateral cross-section of (a) SSFSW joint developed at low traverse speed, (b) SSFSW joint at low rotational speed, (c) CFSW joint developed at low traverse speed, and (d) CFSW joint developed at high traverse speed

was observed at high traverse speed in the case of the CFSW joint (Fig. 5d). The upper part of the NZ, or shoulder active region, in the case of the CFSW joint (Fig. 5c) is wider due to the rotation of the shoulder than the SSFSW joint (Fig. 5a). The shoulder-affected region of the SSFSW joint was found to be narrow due to the use of a small sub-shoulder. The following are two major aspects that can be considered for producing cavity-free SSFSW joints: First, the material movement is focused adjacent to the rotating probe and sub-shoulder, which results in a concentrated flow of material into the weld joint only and helps to produce a cavity-free joint. Second, the material escaping (in the form of flashes) from the weld joint in the case of the CFSW promotes cavity formation, and the SSFSW tool eliminated this problem and hence helped to prevent the cavity formation.

3.2 Metallurgical Analysis

The microstructure of NZ and HAZ was investigated with optical microscopy. The microstructure of the SSFSW and CFSW joints developed at low and high traverse and rotational speeds were analyzed and compared. Refined grains were observed in NZ because of severe plastic deformation and dynamic recrystallization. The microstructure of the NZ and HAZ of SSFSW joints produced at the combinations of 931–13 and 1216–13 is shown in Fig. 6. The distribution of grain size at each speed parameter can be determined from optical micrographs. The matrix grain size of NZ of SSFSW joints produced at speed combinations of 931–13, 931–90, 386–13, and 1216–13 was 1.41 ± 0.14, 1.38 ± 0.13, 1.03 ± 0.13, and 1.91 ± 0.15, respectively. Grain sizes were more influenced by the variation in pin revolving speed than the variation in

traverse speed. Low pin rotation (386 rpm) resulted in a small grain size, while high rotational speed (1216 rpm) resulted in a large grain size. Grains in HAZ are large and unaffected by plastic deformation.

The microstructure of the NZ and HAZ of CFSW joints produced at the combinations of 931–13 and 1216–13 is shown in Fig. 7. The α-Al matrix grain size of NZ of CFSW joints produced at 931–13, 931–90, 386–13, and 1216–13 was 2.01 ± 0.34, 1.73 ± 0.35, 1.24 ± 0.13, and 3.09 ± 0.48 μm, respectively. Grain sizes were significantly influenced by the alteration of rotational speed. The effect of the change in traverse speed in the case of the CFSW joint on grain size was marginal but greater than that of the SSFSW joint. Low rotational speed (386 rpm) resulted in a small grain size, while high rotational speed (1216 rpm) resulted in a large grain size. The FESEM image of base metal (AA2024) is shown in Fig. 8(a). It shows the precipitates present at grain boundaries. An enlarged view of second-phase particles present at the grain boundary is shown in Fig. 8(b). Results obtained from the EDS examination of particles existing at the grain boundary are shown in Fig. 8(c). Copper and magnesium were found to be the key alloying elements within the aluminum matrix. EDS analysis suggested the occurrence of Al_2CuMg (S-phase) as a major precipitate in this alloy.

3.3 Microhardness Study

The microhardness of SSFSW and CFSW joints was examined in the lateral direction of the weld. Microhardness profiles of SSFSW joints at disparate traverse and rotational speeds are displayed in Fig. 9(a) and (b), respectively. The highest hardness (122 HV) was measured in NZ of SSFSW
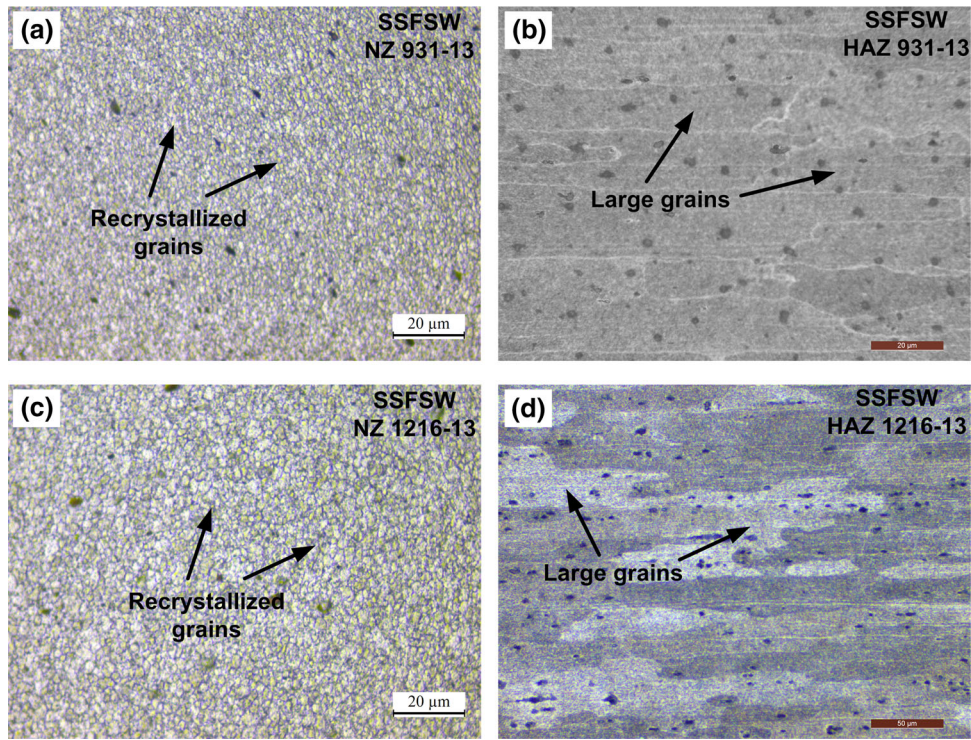
Fig. 6 Optical micrographs of SSFSW joints showing (a) nugget zone, (b) HAZ at 931 rpm–13 mm/min, and (c) nugget zone, (d) HAZ at 1216 rpm–13 mm/min
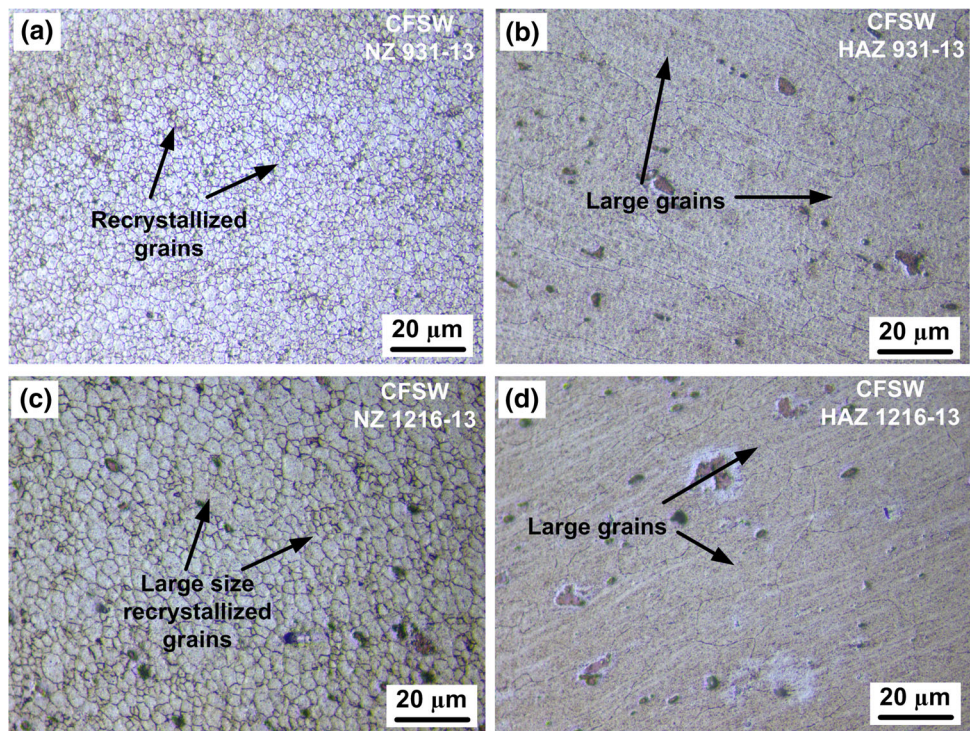

Fig. 7 Optical micrographs of CFSW joints showing (a) nugget zone, (b) HAZ at 931 rpm–13 mm/min, and (c) nugget zone, (d) HAZ at 1216 rpm–13 mm/min

joints produced at 90 mm/min among all different traverse speed samples, while the lowest hardness (85 HV) was measured in HAZ of SSFSW joints produced at 13 mm/min. In the case of different rotational speed samples, the highest hardness (99.7 HV) was measured in the NZ of SSFSW joints produced at 931 rpm, while the lowest hardness (84 HV) was measured in the HAZ of SSFSW joints produced at 386 rpm. Significant variation in the microhardness value of SSFSW
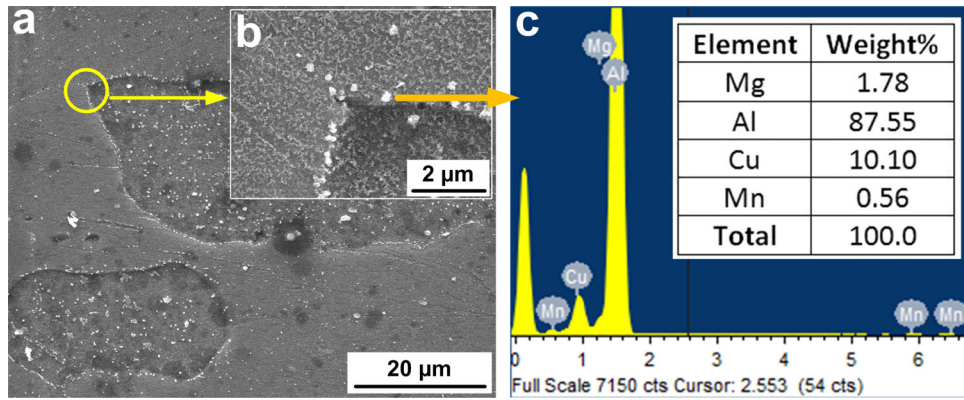
Fig. 8 FESEM images of base metal AA2024 (a) at low magnification, (b) at high magnification showing area inside the circle shown in image 'a', and (c) EDS investigation of second-phase particles exist at grain boundary shown in image 'b'
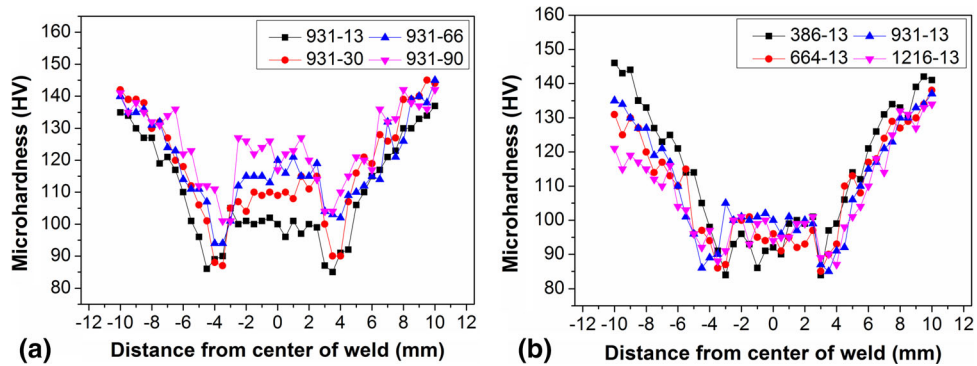
Fig. 9 Microhardness profiles of SSFSW joints of AA2024 at (a) different traverse speeds, and (b) different rotational speeds
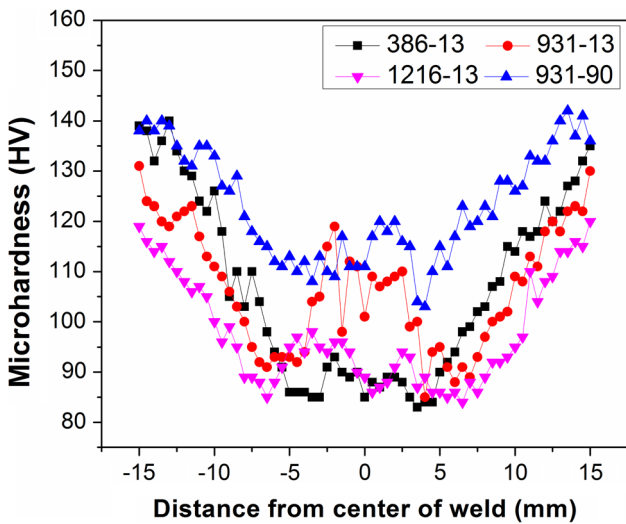

Fig. 10 Microhardness profiles of conventional FSW joint of AA2024 at various traverse and rotational speed parameters

joints was found at different traverse speeds, while the value of microhardness in the case of different rotational speed samples was close to each other. The SSFSW joints produced at constant traverse speed (different rotational speeds) resulted in lower hardness than the sample obtained at different traverse speeds (constant rotational speed).

The microhardness profiles of CFSW joints are presented in Figure 10. The highest hardness (114 HV) was found in NZ of the CFSW joint produced at 931-90 mm/min, while the lowest hardness (83 HV) was found in HAZ of the CFSW joint produced at 386 rpm among the samples produced at all speed parameters. Similar to SSFSW joints, the variation in microhardness value of CFSW joints produced at different traverse speeds was greater than the variation at different rotational speeds. In both cases (SSFSW and CFSW), weld joints produced at 931-90 mm/min resulted in high hardness, while weld joints produced at 386-13 mm/min resulted in low hardness. The HAZ of the CFSW joint comprised a wide low-hardness region (Fig. 10). In the case of the SSFSW joint, hardness approached the base metal level after a narrow region (about 6 mm from the edge of NZ), which suggested a narrow HAZ. On the other hand, in the case of CFSW joints, hardness approached the base metal level after a wide region (about 11 mm from the edge of NZ) suggested a wide HAZ. The SSFSW joint experienced a steep increase in hardness just after crossing the NZ. On the other hand, the CFSW joint experienced a gradual rise in hardness after NZ.

3.4 Tensile Test

Fresh and tested tensile samples extracted from the SSFSW and CFSW joints are shown in Fig. 11. Most of the samples of SSFSW joints were fractured at the interface of the nugget zone and thermo-mechanical affected zone. Stress-strain curves obtained from the SSFSW joints produced at disparate traverse and rotational speeds are shown in Fig. 12(a) and (b),
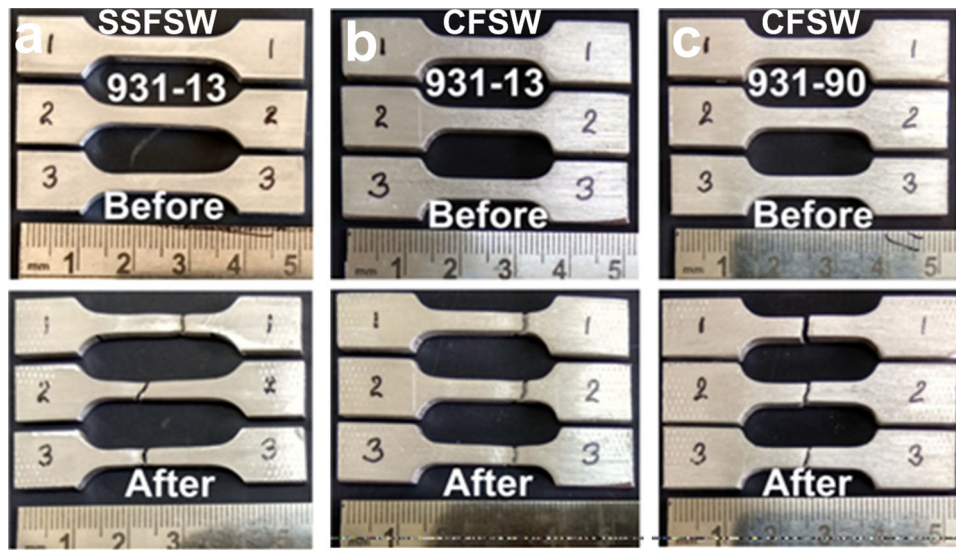
Fig. 11 Tensile samples of (a) SSFSW joint at 931 rpm–13 mm/min, (b) CFSW joint at 931 rpm–13 mm/min and (c) at 931 rpm–90 mm/min
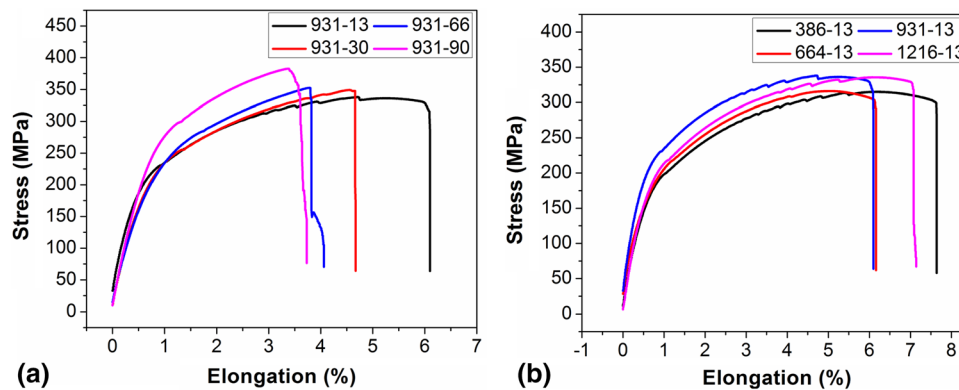
Fig. 12 Stress-strain curves of SSFSW joints of AA2024 at (a) different traverse speeds, and (b) different rotational speeds

respectively. High UTS was obtained at 931-90 mm/min among the different traverse speed weld joints, while low UTS was obtained at 931-13 mm/min. The trend of variation in percentage elongation was opposite to the UTS variation, and low ductility was observed at 931-90 mm/min. A high UTS was obtained at 931-13 mm/min among the different pin rotary speed weld joints, while a low UTS was obtained at 386-13 mm/min. In this case, a high percentage of elongation was obtained at 386-13 mm/min. Tensile properties, including UTS, YS, and elongation (%) of SSFSW joints at various speed parameters, are given in Table 4. UTS and YS were significantly enhanced with an increase in traverse speed. However, percentage elongation was reduced with a rise in traverse speed. However, no particular trend was noticed during the change in pin rotation speed (at fixed traverse speed). However, a marginal difference in the values of strength and ductility was noticed for the weldments developed at disparate rotational speeds. The UTS was enhanced with a rise in the rotational speed, but no significant variation was found at high rotational speeds (i.e., 931 rpm and 1216 rpm). Fractographs obtained from the fractured surface of tensile-tested samples of SSFSW and CFSW joints produced at 386 rpm-13 mm/min are shown in Fig. 13(a) and (b), respectively. All the samples extracted from SSFSW joints at different speed parameters were fractured

in a ductile manner. Dimples present in the fractographs (Fig. 13) are evidence of ductile fracture. The large numbers of fine dimples noticed on the fractured faces of the joints produced at 386 rpm – 13 mm/min are in agreement with the high ductility of these samples.

All the samples prepared from CFSW joints were fractured from HAZ (far from NZ), except the weld developed at 931 rpm – 90 mm/min (Fig. 11c). A sample prepared from a CFSW weld developed at 931 rpm – 90 mm/min was fractured in the NZ. A defect was observed in the macrostructure of the joint when it developed at 90 mm/min (Fig. 5d). Therefore, this joint failed in the NZ at a lower strength than the remaining joints.

Stress-strain curves obtained from the tensile tests of CFSW joints of AA2024 produced at 931 rpm, 386 rpm, and 1216 rpm (at 13 mm/min) are shown in Fig. 14. The curve obtained from the defective weld joint (931 rpm–90 mm/min) is not shown due to premature failure of the samples. High UTS and yield strength were obtained at 931 rpm–13 mm/min. However, percentage elongation was found to be low in the case of 931 rpm–13 mm/min as compared to the remaining parameters. At low and high rotational speeds, marginal variation was found in the UTS value. However, a high percentage of elongation was observed in the FSW joint

Table 4 Tensile properties of SSFSW joint of AA2024 at different speed parameters

Parameters	Traverse speed (mm/min)				Rotational speed (rpm)		
	13	30	66	90	386	664	1216
Ultimate tensile strength, MPa	338 ± 13	349 ± 14	352 ± 14	382 ± 12	315 ± 5	316 ± 9	335 ± 10
Yield strength, MPa	217 ± 12	228 ± 8	234 ± 13	274 ± 9	189 ± 3	193 ± 8	203 ± 3.4
Elongation, %	6.09 ± 0.7	4.66 ± 1.7	4.06 ± 1.8	3.73 ± 1	7.64 ± 0.5	6.16 ± 1.9	7.14 ± 0.5
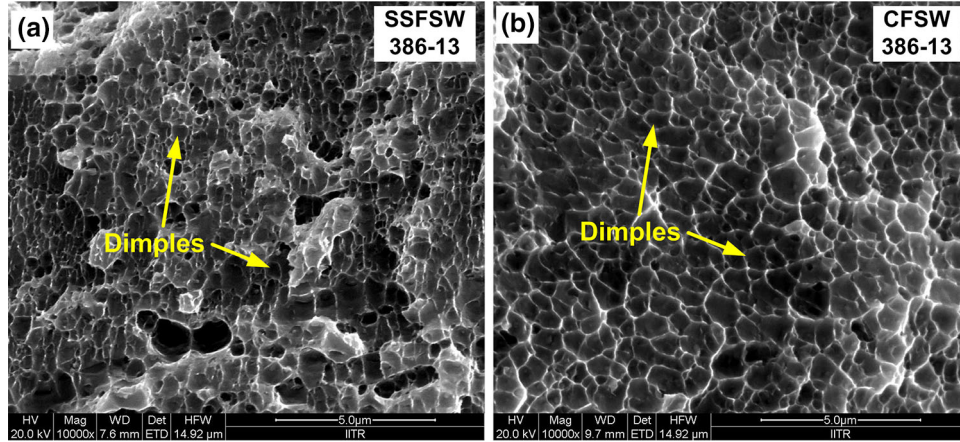
Fig. 13 Fractographs after tensile test of the weld joints produced at 386 rpm–13 mm/min using (a) SSFSW tool, and (b) CFSW tool
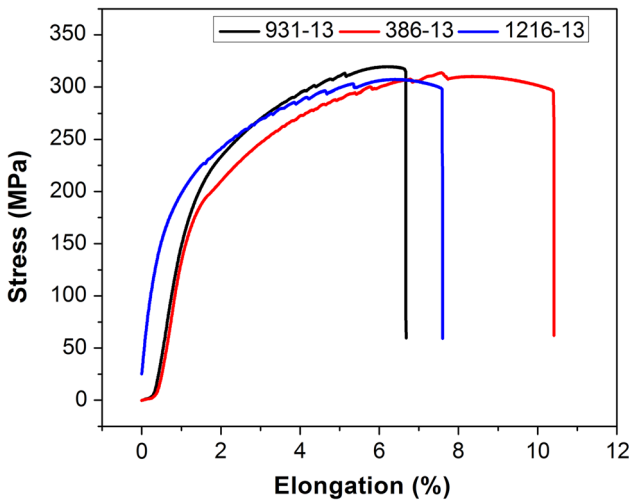
Fig. 14 Stress-strain curves of conventional FSW joints of AA2024 at different speed parameters

produced at 386 rpm. The tensile properties of the CFSW joints of AA2024 produced at different speed parameters are given in Table 5. The UTS of the sound CFSW joints produced at various speed parameters were found to be close to each other. The fractograph obtained from the fractured surface of tensile-tested samples of CFSW joints at 386 rpm – 13 mm/min is shown in Fig. 13(b). All the weld joints were fractured in a ductile manner. Large numbers of small dimples were observed at the fractured surface of the weld joint produced at 386 rpm (Fig. 13b). This observation is also in line with the high ductility obtained from the tensile test of the CFSW joint produced at 386 rpm.
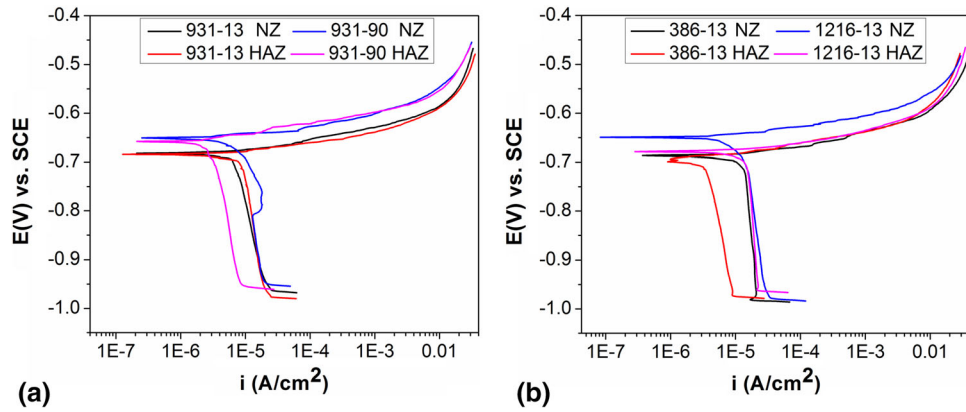
3.5 Corrosion test

A corrosion test (Tafel) of NZ and HAZ of SSFSW joints of AA2024 was performed on samples produced at different speed parameters. Samples were prepared and tested in the same conditions and at the same parameters. All the tests were carried out in an electrolytic solution containing 3.5% NaCl. Curves obtained from the Tafel test of NZ and HAZ of SSFSW joints produced at 931 rpm (13 mm/min and 90 mm/min) and 13 mm/min (386 rpm and 1216 rpm) are displayed in Fig. 15(a) and (b), respectively. Low corrosion potential (more negative) was observed at a minimum traverse speed (13 mm/min) compared to the maximum transverse speed (90 mm/min). This indicates the low corrosion resistance of the SSFSW joint produced at 931 rpm–13 mm/min. A low corrosion potential (more negative) was shown by the Tafel curve (Fig. 15b) obtained from the sample produced at a low rotational speed (386 rpm) than at a high rotational speed (1216 rpm). Thus, low corrosion resistance was exhibited by the SSFSW joint produced at 386 rpm–13 mm/min. Corrosion potentials (E_{corr}) obtained from Tafel tests of NZ and HAZ of SSFSW welds developed at disparate speed parameters are shown in Table 6. The corrosion potential was enhanced with a rise in traverse and rotational speeds, which in turn improved the corrosion resistance, and vice versa. In all cases, lower corrosion resistance was observed in HAZ than in NZ. A significant difference was observed between the corrosion potential of NZ and HAZ of SSFSW welds produced at maximum rotational speed (1216 rpm).

Scanning electron microscopic images of the corroded surface of NZ and HAZ of SSFSW welds developed at low and high traverse speeds (at 931 rpm) are shown in Fig. 16. Pitting corrosion was observed in all the cases. The corrosion attack was much more severe in the case of HAZ than the NZ. Severe

Table 5 Tensile properties of conventional FSW joint of AA2024 at different speed parameters

Parameters	Traverse speed, mm/min		Rotational speed, rpm	
	13	90	386	1216
Ultimate tensile strength, MPa	319 ± 7.5	170 ± 5.1	313 ± 7.5	307 ± 12
Yield strength, MPa	197 ± 10	163 ± 6	181 ± 7.8	178 ± 4
Elongation, %	6.67 ± 1.5	1.54 ± 0.3	10.41 ± 0.7	7.59 ± 1.4

Fig. 15 Tafel curves acquired from corrosion test of NZ and HAZ of SSFSW joints of AA2024 produced at (a) different traverse speeds, and (b) different rotational speeds

Table 6 Corrosion potential (mV) of NZ and HAZ of SSFSW joints of AA2024 at different speed parameters

Parameters	Traverse speed, mm/min		Rotational speed, rpm	
	13	90	386	1216
Nugget zone, mV	− 682	− 651	− 687	− 649
Heat-affected zone, mV	− 684	− 658	− 696	− 679

pitting was witnessed in the cases of NZ and HAZ of the sample produced at a low rotational speed, i.e., 386 rpm, compared to the high rotational speed, i.e., 1216 rpm. Hence, the analysis of the corroded surface is in agreement with the result of the potentiodynamic polarization test of SSFSW joints.
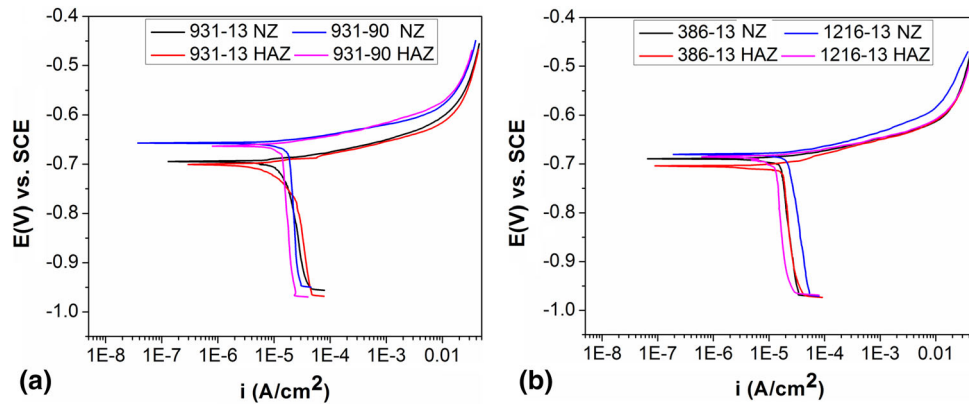
The NZ and HAZ of the CFSW joints of AA2024 were tested using the same criteria and circumstances as the SSFSW joints. The curves obtained through the Tafel test of NZ and HAZ of conventional joints produced at 931 rpm (at 13 mm/min and 90 mm/min) and 13 mm/min (at 386 rpm and 1216 rpm) are shown in Fig. 17(a) and (b), respectively. Low corrosion potential (more negative) was observed at a minimum traverse speed (13 mm/min) compared to the maximum traverse speed (90 mm/min). It indicated the lower corrosion resistance of the sample produced at a low traverse speed than at a high traverse speed. A low corrosion potential was also observed at a slower rotational speed than at the faster rotational speed, which indicated less corrosion resistance in the sample developed at a lower rotational speed. The E_{corr} acquired from the potentiodynamic polarization test of NZ and HAZ of the CFSW joint is given in Table 7. An increase in the traverse and rotational speeds increased the corrosion resistance. HAZ resulted in lower corrosion resistance than NZ.

Contrary to the result of the SSFSW joint at high rotational speed (1216 rpm), the marginal difference between the corrosion potential of NZ and HAZ was found in the case of the CFSW joint. The HAZ of the CFSW joint at various speed parameters showed more pitting than the NZ (Fig. 18). The weld joint produced at a lower traverse speed showed more pitting than the one produced at a higher traverse speed. Although the results obtained from the corrosion test of CFSW joints showed a similar trend to the SSFW joints, the corrosion potential of CFSW joints was more negative than that of the SSFSW welds. It suggested the high corrosion resistance of SSFSW joints compared to CFSW joints. These results are in agreement with the previous study on the corrosion behavior of the SSFSW joint of AA2014 aluminum alloy at a fixed speed parameter (Ref 27).

The stationary shoulder tool was found to be very effective in producing sound weld joints at a wide range of speed parameters. SSFSW joints were found free of tunnel defects. The variation of the tool tilt angle is outside the scope of the present paper; however, the authors want to mention that the current SSFSW tool is also capable of producing sound weld joints at different tilt angles and can be a part of future work. The conventional tool produced defective joints, especially at
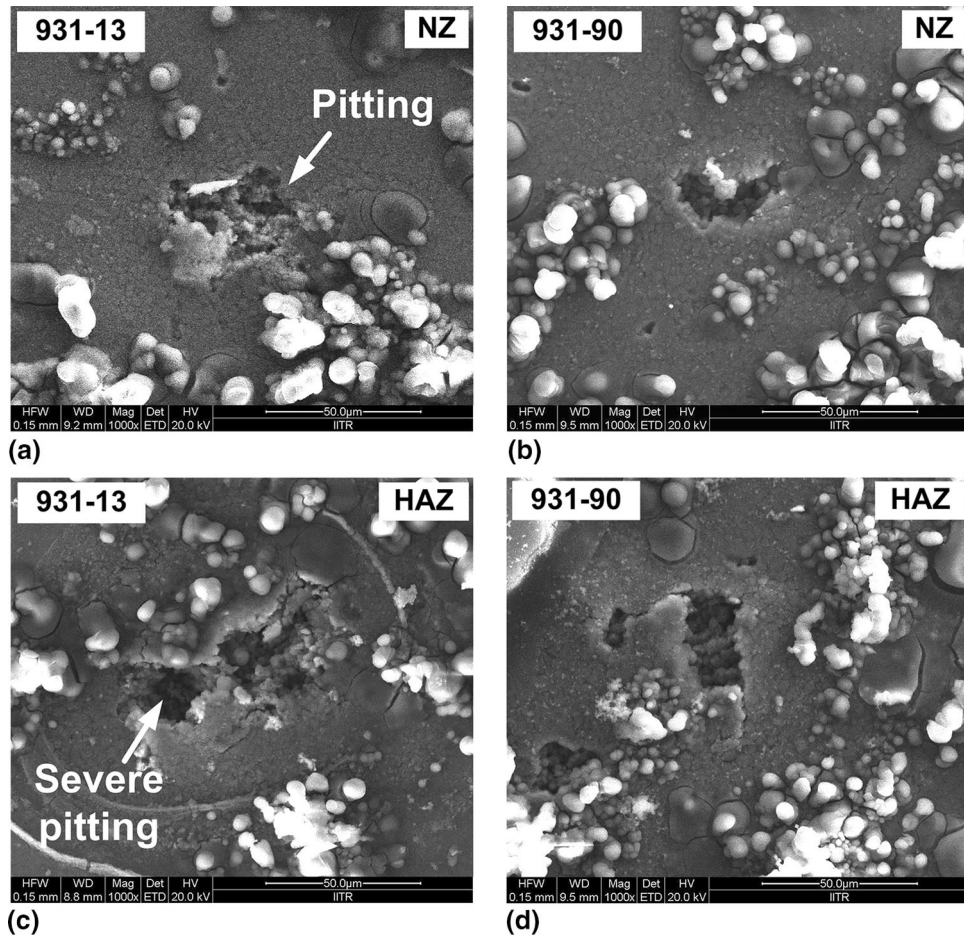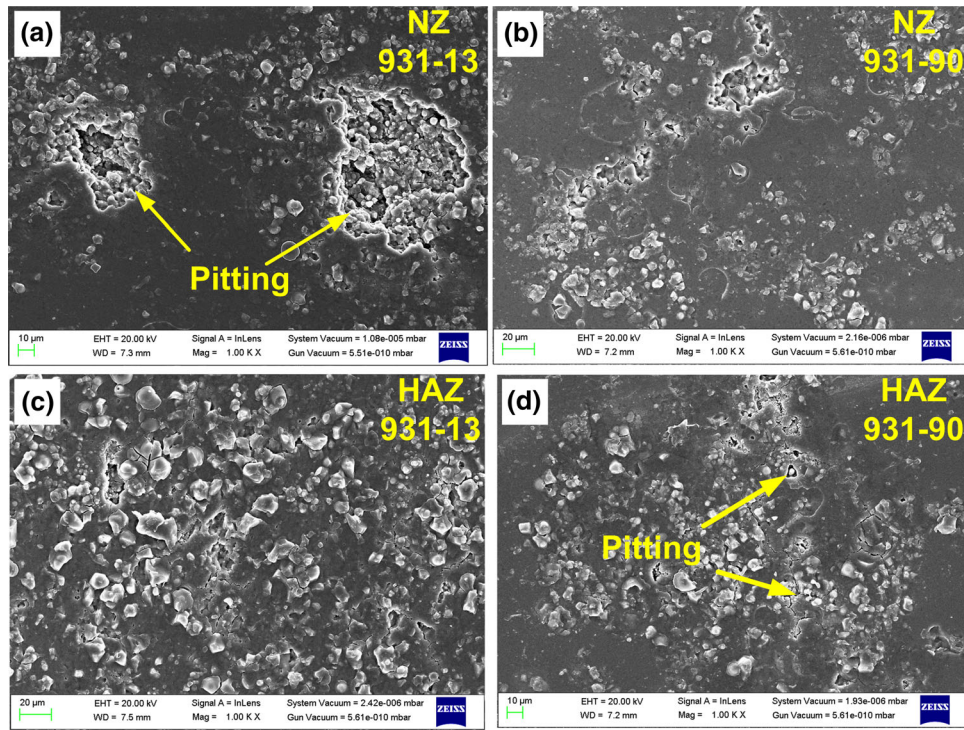
Fig. 16 Corroded surfaces of SSFSW joints obtained from (a) NZ at low traverse speed, (b) NZ at high traverse speed, (c) HAZ at low traverse speed, and (d) HAZ at high traverse speed

Fig. 17 Tafel curves acquired from the corrosion test of NZ and HAZ of CFSW joints of AA2024 produced at (a) different traverse speeds, and (b) different rotational speeds

Table 7 Corrosion potential (mV) of NZ and HAZ of conventional FSW joints of AA2024 at different speed parameters

Parameters	Traverse speed, mm/min			Rotational speed, rpm	
	13	90		386	1216
Nugget zone, mV	− 695	− 657		− 690	− 681
Heat-affected zone, mV	− 701	− 664		− 704	− 685

Fig. 18 Corroded surfaces of CFSW joints obtained from (a) NZ at low traverse speed, (b) NZ at high traverse speed, (c) HAZ at low traverse speed, and (d) HAZ at high traverse speed

low tool tilt angles during variations of the tool tilt angles described in the literature (Ref 28). The upper surface of the SSFSW welds was found to be smooth without arc corrugation. Transverse cross-sections of SSFSW joints exhibited minor asymmetry in NZ as compared to the CFSW joints.

The stationary shoulder tool generates less heat during welding than the CFSW tool. An increase in the width of the NZ at reduced traverse speed can be credited to the augmented heat input as well as the high strain rate. Fine grains in the NZ of SSFSW joints were attributed to the low heat input (Ref 29). The major strengthening precipitate in AA2024 was Al_2CuMg. The dislocation density also affects the mechanical properties of the joint, and SSFSW reduced the dislocation density, as reported in the literature (Ref 30). The comparative effect of SSFSW with conventional FSW on dislocation density needs to be studied in future. Microhardness profiles confirmed the reduction in the low-hardness region in SSFSW joints compared to CFSW joints. A major motive to develop the present stationary shoulder tool was achieved through the reduction in the width of HAZ. The SSFSW tool reduced the low-hardness band by almost half as compared to the CFSW tool. The overall microhardness of the SSFSW joint was also improved. High traverse as well as rotational speeds were found to be effective in improving the microhardness of SSFSW joints.

The SSFSW tool resulted in high UTS at all the speed parameters used in the current study. The increase in traverse speed reduced the width of HAZ, which in turn improved the tensile strength of the SSFSW joints, as reported in the literature (Ref 31). The decrease in ductility of SSFSW joints can be attributed to the reduction in the soft region in HAZ. The CFSW tool was not capable of producing a sound weld joint at 90 mm/min (931 rpm), whereas the stationary shoulder tool resulted in higher strength at 90 mm/min than the other

parameters. In the literature, the change in UTS was found to be more sensitive to variation in traverse speed than the rotational speed for the SSFSW joint of 6xxx series aluminum alloy, and the results of the present study also show a similar trend (Ref 32). The fracture locations of tensile samples are in agreement with microhardness profiles. In both the cases, fracture location of FSW joints shifted according to the low-hardness region in both cases. It was shifted far away from the NZ in the case of the CFSW joint. The refined microstructure resulted in improved hardness as well as tensile strength in the case of the SSFSW joint. The coarsening and dissolution of the precipitates in the HAZ drastically reduced the strength and hardness of the region. Therefore, the change in microstructure due to the plastic deformation and thermal cycle significantly affected the strength and microhardness of the joint (Ref 33).

The electrochemical behavior of the AA2024 aluminum alloy becomes complex due to the presence of copper. Pitting corrosion is the major electrochemical phenomenon associated with aluminum alloys that contain precipitates in their microstructure. The nature of the second-phase particles strongly affects the corrosion resistance of the aluminum alloy (Ref 34). The aluminum matrix and the S-phase (Al_2CuMg) exhibit different electrochemical behavior. The potential difference between the matrix and S-phase is a key reason to initiate the corrosion process. The potential of the Al_2CuMg precipitate was found to be negative as compared to the aluminum matrix, which indicated the anodic behavior of Al_2CuMg precipitates (Ref 35). The presence of magnesium in the S-phase resulted in more negative potential. Thus, preferably, the precipitate was dissolved during the corrosion and resulted in pit formation. No trenching was observed on the corroded surface. Most of the time, trenching occurs when precipitate acts as a cathode with respect to surroundings. Aluminum is a highly reactive material, and it forms a layer of oxide film by reacting

with the environment (Ref 36). Fine grain size favors the formation of a passive oxide layer and, hence, helps to reduce the corrosion attack (Ref 37). A direct relationship between grain size and corrosion attack has been reported, where fine grain structure was found to be more corrosion resistant in the friction stir-processed region (Ref 38). The SSFSW weld exhibited fine grains in comparison with the CFSW weld, which in turn helped to improve the corrosion resistance. Therefore, the tool with a stationary shoulder enhanced the corrosion resistance and reduced the corrosion-sensitized region (i.e., HAZ) as compared to the CFSW tool.

4. Conclusions

The stationary shoulder FSW of AA2024 aluminum alloys is executed at numerous speed parameters using an indigenously designed SSFSW tool. The influence of the SSFSW tool on the microstructure, microhardness, tensile strength, and corrosion resistance of weld joints could be concluded as follows:

(1) The SSFSW tool is capable of producing a sound weld joint at a wide range of speed parameters (386-1216 rpm and 13-90 mm/min.) with a near-symmetrical shape of the nugget zone.
(2) A significant change in the width of the nugget zone of the SSFSW joint is observed with variations in traverse speed. The reduction of 16% in the width of the nugget zone is attained at a change in traverse speed from 13 to 90 mm/min.
(3) The nugget zone exhibits equiaxed grains due to plastic deformation and dynamic recrystallization. The matrix grain size in the nugget zone is increased from 1.03 ± 13 to 1.91 ± 0.15 μm with an increase in rotational speed from 386 to 1216 rpm.
(4) The microhardness significantly decreases in HAZ than in NZ. The low-hardness region (HAZ) is shifted toward NZ in the SSFSW joint. The highest hardness is obtained at 90 mm/min in NZ (122 HV), while the lowest is obtained by the sample produced at 386 rpm in HAZ (84 HV).
(5) UTS increases with an increase in traverse speed from 13 to 90 mm/min. The tensile strength exhibits an increasing trend with an increase in rotational speed, followed by a decreasing trend with a further increase in rotational speed. The fracture location is the HAZ and moves as the soft region changes with the variation in parameters.
(6) The HAZ is observed as the most severely corrosion-prone region in the SSFSW joints. The SSFSW tool successfully reduces the width of this region and, hence, improves the corrosion resistance of the joint.
(7) The HAZ is noticed as the region that degrades the performance of the SSFSW joint, and the results obtained from microhardness, tensile, and corrosion tests confirm this observation.

Conflict of interest

Authors declare that there is no conflict of interest with respect to authorship, research or publication of this article.

References

1. P. Goel, N.Z. Khan, Z.A. Khan, A. Ahmari, N. Gangil, M.H. Abidi, and A.N. Siddiquee, Investigation on Material Mixing during FSW of AA7475 to AISI304, *Mater. Manuf. Processes*, 2019, **34**(2), p 192–200.
2. N. MohdSelamat, A. Hossein Baghdadi, Z. Sajuri, A.H. Kokabi, and S. Junaidi, Effect of Rolling on Strength of Friction Stir Welded Joint of Aluminium Alloys, *Jurnal Kejuruteraan*, 2018, **sil**(6), p 9–15. https://doi.org/10.17576/jkukm-2018-si1(6)-02
3. N.F.M. Selamat, A.H. Baghdadi, Z. Sajuri, S. Junaidi, and A.H. Kokabi, Rolling Effect on Dissimilar Friction Stir Welded AA5083-AA6061 Aluminium Alloy Joints, *J. Adv. Manuf. Technol.*, 2020, **14**, p 49–62.
4. N.F.M. Selamat, A.H. Baghdadi, Z. Sajuri, and A.H. Kokabi, Weldability and Mechanical Properties of Dissimilar Al-MgSi to Pure Aluminium and Al-Mg Using Friction Stir Welding Process, *J Teknol*, 2019, **81**(1), p 143–149.
5. K.K. Kumar, A. Kumar, and M.V.N.V. Satyanarayana, Enhancing Corrosion Resistance and Mechanical Properties of Dissimilar Friction Stir Welded 5083–6061 Aluminium Alloys Using External Cooling Environment, *Proceed. Instit. Mech. Eng., Part L: J. Mater.: Design Appl.*, 2021, **235**(12), p 2692–2708.
6. X. Meng, Y. Huang, J. Cao, J. Shen, and J.F. dos Santos, Recent Progress on Control Strategies for Inherent Issues in Friction Stir Welding, *Prog Mater Sci*, 2021, **115**, p 100706.
7. X. Meng, Y. Xie, S. Sun, X. Ma, L. Wan, J. Cao, and Y. Huang, Lightweight Design: Friction-Based Welding between Metal and Polymer, *Acta. Metallurgica. Sinica (English Letters)*, 2023, **36**(6), p 881–898.
8. S. Rajesh and V. Badheka, Influence of Heat Input/Multiple Passes and Post Weld Heat Treatment on Strength/Electrochemical Characteristics of Friction Stir Weld Joint, *Mater. Manuf. Processes*, 2018, **33**(2), p 156–164.
9. A.H. Baghdadi, Z. Sajuri, A. Keshtgar, N.M. Sharif, and A. Rajabi, Mechanical Property Improvement in Dissimilar Friction Stir Welded Al5083/Al6061 Joints: Effects of Post-Weld Heat Treatment and Abnormal Grain Growth, *Materials*, 2022, **15**(1), p 288.
10. J.P. Martin, "Stationary Shoulder Friction Stir Welding," *Proceedings of the 1st International Joint Symposium on Joining and Welding*, Woodhead Publishing Limited, 2013, p 477–482, doi:https://doi.org/10.1533/9781782421641.477
11. N. Sharma, A.N. Siddiquee, Z.A. Khan, and M.T. Mohammed, Material Stirring during FSW of Al–Cu: Effect of Pin Profile, *Mater. Manuf. Processes*, 2018, **33**(7), p 786–794.
12. Y. Huang, X. Meng, Y. Xie, L. Wan, Z. Lv, J. Cao, and J. Feng, Friction Stir Welding/Processing of Polymers and Polymer Matrix Composites, *Compos Part A Appl Sci Manuf*, 2018, **105**, p 235–257. https://doi.org/10.1016/j.compositesa.2017.12.005
13. Y. Huang, X. Meng, Y. Xie, J. Li, and L. Wan, Joining of Carbon Fiber Reinforced Thermoplastic and Metal via Friction Stir Welding with Co-Controlling Shape and Performance, *Compos Part A Appl Sci Manuf*, 2018, **112**, p 328–336.
14. S. Sinhmar and D.K. Dwivedi, Mechanical Behavior of FSW Joint Welded by a Novel Designed Stationary Shoulder Tool, *Journal of Materials Processing Tech.*, 2020, **277**, p 116482. https://doi.org/10.1016/j.jmatprotec.2019.116482
15. J.P. Martin, C. Stanhope, and S. Gascoyne, Novel Techniques for Corner Joints Using Friction Stir Welding, *Friction Stir Welding and Proceeing VI*, 2011 https://doi.org/10.1002/9781118062302
16. Y. Chen, H. Li, X. Wang, H. Ding, and F. Zhang, A Comparative Investigation on Conventional and Stationary Shoulder Friction Stir Welding of Al-7075 Butt-Lap Structure, *Metals (Basel)*, 2019, **9**(12), p 1264.

17. A. Abdollahzadeh, B. Bagheri, M. Abbasi, F. Sharifi, S.E. Mirsalehi, and A.O. Moghaddam, A Modified Version of Friction Stir Welding Process of Aluminum Alloys: Analyzing the Thermal Treatment and Wear Behavior, *Proceed. Institut. Mech. Eng., Part L: J. Mater.: Design App.*, 2021, **235**(10), p 2291–2309.

18. W. He, M. Li, Q. Song, J. Liu, and W. Hu, Efficacy of External Stationary Shoulder for Controlling Residual Stress and Distortion in Friction Stir Welding, *Transact. Indian Instit. Metals*, 2019, **72**(5), p 1349–1359. https://doi.org/10.1007/s12666-019-01630-2

19. W. He, J. Liu, W. Hu, G. Wang, and W. Chen, Controlling Residual Stress and Distortion of Friction Stir Welding Joint by External Stationary Shoulder, *High Temp. Mater. Processes (London)*, 2019, **2019**(38), p 662–671.

20. V. Patel, W. Li, and Y. Xu, Stationary Shoulder Tool in Friction Stir Processing: A Novel Low Heat Input Tooling System for Magnesium Alloy, *Materials and Manufacturing Processes*, 2018, **34**(2), p 177–182. https://doi.org/10.1080/10426914.2018.1544716

21. Z. Xu, Z. Li, Z. Lv, and L. Zhang, Effect of Welding Speed on Joint Features and Lap Shear Properties of Stationary Shoulder FSLWed Alclad 2024 Al Alloy, *J Mater Eng Perform*, 2017, **26**(3), p 1358–1364.

22. Z. Zhou, Y. Yue, S. Ji, Z. Li, and L. Zhang, Effect of Rotating Speed on Joint Morphology and Lap Shear Properties of Stationary Shoulder Friction Stir Lap Welded 6061–T6 Aluminum Alloy, *Int. J. Adv. Manuf. Technol.*, 2017, **88**(5–8), p 2135–2141. https://doi.org/10.1007/s00170-016-8924-6

23. H. Yang, H. Zhao, X. Xu, L. Zhou, H. Zhao, and H. Liu, Effect of Stirring Pin Rotation Speed on Microstructure and Mechanical Properties of 2A14-T4 Alloy T-Joints Produced by Stationary Shoulder Friction Stir Welding, *Materials*, 2021, **14**(8), p 1938.

24. J. You, Y. Zhao, C. Dong, Y. Yi, and Y. Su, Numerical Modeling of Multiphysics Field in Conventional and Stationary Shoulder Friction Stir Welding of Al-Cu Alloy, *J Mater Eng Perform*, 2021, **30**(4), p 2751–2760. https://doi.org/10.1007/s11665-021-05642-2

25. C. Zhang, Y. Cao, G. Huang, Q. Zeng, and Y. Zhu, Influence of Tool Rotational Speed on Local Microstructure, Mechanical and Corrosion Behavior of Dissimilar AA2024/7075 Joints Fabricated by Friction Stir Welding, *J. Manuf. Process.*, 2019, **2020**(49), p 214–226.

26. D. Sejani, W. Li, and V. Patel, Stationary Shoulder Friction Stir Welding-Low Heat Input Joining Technique: A Review in Comparison with Conventional FSW and Bobbin Tool FSW, *Critical Rev. Solid State Mater. Sci.*, 2021 https://doi.org/10.1080/10408436.2021.1935724

27. S. Sinhmar and D.K. Dwivedi, Art of Friction Stir Welding to Produce Weld Joint without Rotation of Shoulder with Narrow Heat- Affected Zone and High Corrosion Resistance, *Sci. Technol. Weld. Join*, 2020, **25**(6), p 490–495. https://doi.org/10.1080/13621718.2020.1746512

28. K.P. Mehta and V.J. Badheka, Effects of Tilt Angle on the Properties of Dissimilar Friction Stir Welding Copper to Aluminum, *Mater. Manuf. Process.*, 2016, **31**(3), p 255–263.

29. A. Hossein Baghdadi, N. Fazilah, M. Selamat, Z. Sajuri, and A.H. Kokabi, Effect of Travel Speed on Quality and Welding Efficiency of Friction Stir Welded AZ31B Magnesium Alloy, *International Journal of Engineering & Technology*, 2018, **7**, p 94–99, www.sciencepubco.com/index.php/IJET

30. W. Li, P.L. Niu, S.R. Yan, V. Patel, and Q. Wen, Improving Microstructural and Tensile Properties of AZ31B Magnesium Alloy Joints by Stationary Shoulder Friction Stir Welding, *J. Manuf. Process.*, 2019, **37**, p 159–167.

31. H. Wu, Y.C. Chen, D. Strong and P. Prangnell, Stationary Shoulder FSW for Joining High Strength Aluminum Alloys, *J. Mater. Process. Technol.*, 2015, **221**, p 187–196.

32. D. Li, X. Yang, L. Cui, F. He, and H. Shen, Effect of Welding Parameters on Microstructure and Mechanical Properties of AA6061-T6 Butt Welded Joints by Stationary Shoulder Friction Stir Welding, *Mater. Des.*, 2014, **64**, p 251–260.

33. O.S. Salih, N. Neate, H. Ou, and W. Sun, Influence of Process Parameters on the Microstructural Evolution and Mechanical Characterisations of Friction Stir Welded Al-Mg-Si Alloy, *J Mater Process Technol*, 2020, **2020**(275), p 116366.

34. M. Zhang, M. Paidar, O.O. Ojo, S. Mehrez, S. Narayanasamy, A.M. Zain, and V. Mohanavel, Impact of Multiple FSP Passes on Structure, Mechanical, Tribological and Corrosion Behaviors of AA6061/316 Stainless-Steel Reinforced Al Matrix Composites, *Surf Coat Technol*, 2022, **447**, p 128801.

35. A. Hughes E., N. Birbilis, J. M.C., S. J., X. Zhou, and G. E., High Strength Al-Alloys: Microstructure, Corrosion and Principles of Protection, *Recent Trends in Processing and Degradation of Aluminium Alloys*, Zaki Ahmad, Ed., InTech, 2011, p 223–262, doi:https://doi.org/10.5772/18766

36. J.R. Davis, "Corrosion of Aluminum and Aluminum Alloys," Asm International, 1999

37. T.S. Srivatsan, T.S. Sudarshan, and G.E. Bobeck, Corrosion Behaviour of a Quaternary AI-Li-Cu-Mg Alloy in 3.5% NaCI Solution, *Br. Corr. J.*, 2013, **25**(1), p 39–45.

38. S. Liu, M. Paidar, O. OladimejiOjo, M.Š Poková, S. Mehrez, A.M. Zain, Q. Zhao, and J. Wang, Friction Stir Processing of Hybridized AZ31B Magnesium Alloy-Based Composites by Adding CeO_2 and ZrO_2 powders: Mechanical Wear, and Corrosion Behaviors, *J. Mater. Res. Technol.*, 2023, **24**, p 1949–1972.